

# Three-Dimensional Segmentation and Growth-Rate Estimation of Small Pulmonary Nodules in Helical CT Images

William J. Kostis\*, *Member, IEEE*, Anthony P. Reeves, *Senior Member, IEEE*, David F. Yankelevitz, and Claudia I. Henschke

**Abstract**—Small pulmonary nodules are a common radiographic finding that presents an important diagnostic challenge in contemporary medicine. While pulmonary nodules are the major radiographic indicator of lung cancer, they may also be signs of a variety of benign conditions. Measurement of nodule growth rate over time has been shown to be the most promising tool in distinguishing malignant from nonmalignant pulmonary nodules. In this paper, we describe three-dimensional (3-D) methods for the segmentation, analysis, and characterization of small pulmonary nodules imaged using computed tomography (CT). Methods for the isotropic resampling of anisotropic CT data are discussed. 3-D intensity and morphology-based segmentation algorithms are discussed for several classes of nodules. New models and methods for volumetric growth characterization based on longitudinal CT studies are developed. The results of segmentation and growth characterization methods based on *in vivo* studies are described. The methods presented are promising in their ability to distinguish malignant from nonmalignant pulmonary nodules and represent the first such system in clinical use.

**Index Terms**—Classification, mathematical morphology, moments, pulmonary nodules, segmentation.

## I. INTRODUCTION

THE pulmonary nodule is a radiographic finding that is now of particular importance given the burgeoning interest in early detection of lung cancer using computed tomography (CT). Pulmonary nodules may represent a variety of benign disease, necessitating little intervention, to a host of malignant pathologies requiring early intervention to avert mortality. The expeditious differential diagnosis of these lesions is critical, as the mortality of traditionally detected lung cancer is over 90% [1].

Computer vision methods for the analysis of pulmonary nodules in CT scans have, until recently, relied on two-dimensional (2-D) measurements of the single image considered to best represent the lesion. One of the issues has been the anisotropic

nature of tomographic images, especially those produced in full-lung scans in which nodules are detected. In such scans, the resolution in the axial dimension is typically 10–20 times more coarse than the in-plane resolution. Another reason for the use of 2-D metrics is that these lesions have traditionally been detected, measured, and characterized on chest radiographs. The extension of these 2-D methods to a newer imaging modality was more intuitive to most radiologists.

Two-dimensional metrics have been used in both refining nodule candidates in detection algorithms, as well as in the analysis of identified nodules, toward the prediction of malignancy. Giger *et al.* [2] reported the early use of automated 2-D nodule metrics, including perimeter, area, compactness, and circularity. Toshioka *et al.* [3] later added mean density and variation measures. Texture measures were used by McNitt-Gray *et al.* [4]. 2-D nodule segmentation and growth analysis has also been described [5], [6].

More recently, three-dimensional (3-D) measures of nodule volume, shape, and surface characteristics have been described in the literature [7]–[11]. Work has also been reported on classification systems that rely on nodule feature characterization in contrast-enhanced CT [12], [13].

The advent of multidetector scanners with high resolution and fast acquisition time have now enabled 3-D analysis of nodules from both focused scans of a particular region and, to some extent, nodules detected in full-lung screening studies. Significant work is also being done in automatic localization of nodules on repeat CT studies. Brown *et al.* have described a system based on fuzzy matching of automatically segmented anatomic regions [14]. In the paper by Ko and Betke, following identification of the nodule location in the second scan, volumetric estimates are extrapolated from 2-D diameter measurements and ternary classification of size change (decrease, stable, increase) is determined [15].

One of the best predictors of nodule malignancy is growth rate. Similarly, nodule size is also highly correlated with malignancy. Significantly larger nodules (>3 cm in diameter) are more likely to represent lung cancer [16]. Overall size has, therefore, been used in characterization and classification studies [16], [17]. Our interest, however, is to characterize nodules as early as possible, i.e., when they are still small in size (less than 10 mm in diameter). This motivates the use of *size-invariant measures*, those that are independent of overall size. The most notable of these is an estimate of the nodule growth rate or *doubling time*.

Manuscript received May 2, 2002; revised May 3, 2003. This work was supported in part by the National Institutes of Health under Grant R01-CA-63393 and Grant R01-CA-78905. The Associate Editor responsible for coordinating the review of this paper and recommending its publication was W. Niessen. Asterisk indicates corresponding author.

\*W. J. Kostis is with the Department of Radiology, Weill Medical College, Cornell University, New York, NY 10021 USA (e-mail: wjk2001@med.cornell.edu).

A. P. Reeves is with the School of Electrical and Computer Engineering, Cornell University, Ithaca, NY 14853 USA.

D. F. Yankelevitz and C. I. Henschke are with the Department of Radiology, Weill Medical College, Cornell University, New York, NY 10021 USA.

Digital Object Identifier 10.1109/TMI.2003.817785

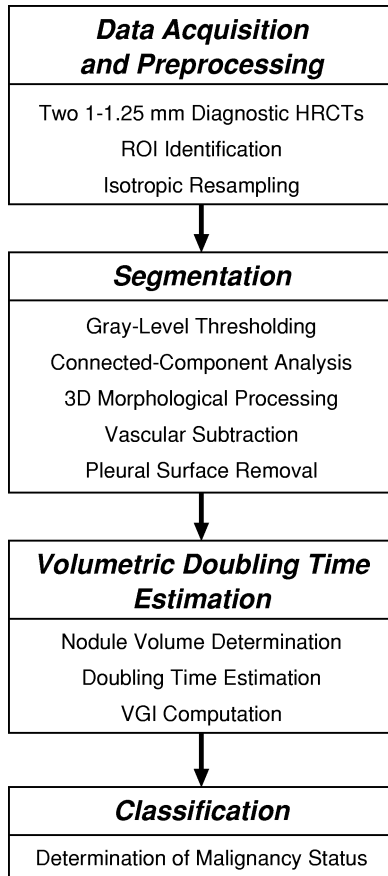


Fig. 1. Overview of the system developed.

In this paper, we describe 3-D methods for volumetric doubling-time estimation in small pulmonary nodules seen in high-resolution CT images. Previous efforts by our group in 2-D and 3-D nodule segmentation and growth analysis have been reported [5], [6], [8], [11]. This work was first based on  $k$ -means and gradient-based segmentation techniques and later led to improved methods, as well as a variety of measures to be used in evaluating and improving the accuracy of nodule segmentation. The 3-D segmentation methods in this paper are model-based and implemented with techniques from mathematical morphology. An overview of the entire system developed is illustrated in Fig. 1.

## II. NODULE MODELS

The radiographic appearance of pulmonary nodules in CT images can be described as compact opaque lesions with attenuation near or slightly higher than that of water ( $\sim 0$ –100 HU). A small pulmonary nodule is (usually) roughly spherical, with a diameter less than 1 cm. The nodule has a density (CT attenuation) significantly higher than that of the surrounding lung parenchyma. The nodule form may be confounded by other neighboring/attached structures, including vessels and the pleural surface. Segmentation and subsequent analysis of these lesions is predicated upon formal models of several distinct classes of pulmonary nodules based on their position in the lung and surrounding structures. We may define four classes of pulmonary nodules as follows.

- 1) *Well-circumscribed*: The nodule is located centrally in the lung, without significant connections to vasculature.
- 2) *Vascularized*: The nodule is located centrally in the lung, but has significant vascularization (connections to neighboring vessels).
- 3) *Pleural tail*: The nodule is near the pleural surface, connected by a thin structure (“pleural tail”).
- 4) *Juxtapleural*: A significant proportion of the nodule periphery is connected to the pleural surface.

A review of 200 nodules in our clinical database revealed that nearly half of the nodules were vascularized, approximately one-third were well circumscribed, nearly one-quarter were juxtapleural, and a small minority (approximately 1%) had pleural tails.

Techniques for the segmentation of each of these nodule classes differ as the varied local geometry is not amenable to a single method. We may, therefore, formulate mathematical models of each class and develop separate segmentation schemes accordingly. In this discussion, it is assumed that the image under consideration is the 3-D region of interest (ROI) containing the nodule. The models corresponding to each of these nodule classes are illustrated graphically along with CT examples of *in vivo* nodules, as shown in Fig. 2.

### A. Well-Circumscribed Nodule

A well-circumscribed nodule is one that is located centrally in the lung without significant connections to vasculature, as illustrated in Fig. 2(a), where the nodule region  $N$  is distinct from the surrounding lung parenchyma  $LP$ . A CT image representing the central axial slice of a well-circumscribed pulmonary nodule is shown in Fig. 2(b).

The nodule consists of tissue exhibiting a higher X-ray attenuation and, therefore, voxel intensity, than the surrounding lung parenchyma. We model it by the set  $N$  of voxels in the nodule that are greater than or equal to a given intensity threshold  $T$  as follows:

$$N = \{v(x, y, z) | v(x, y, z) \geq T\}. \quad (1)$$

Such a model would be very sensitive to noise, however, as any voxel in the ROI meeting the threshold criterion would be included. A better model would include connectivity between the voxels in the nodule. For each voxel in the set, there would need to be at least one neighboring voxel also in the set. We also exclude the trivial case where the nodule would be a single voxel. This connected nodule model could be defined in terms of the set of voxels adjacent to a given voxel, denoted as  $\text{adj}(v(x, y, z))$ . Our model for the well-circumscribed nodule is then the set of connected voxels greater than or equal to a given intensity threshold as follows:

$$N_c = \{v(x, y, z) | (v(x, y, z) \geq T) \wedge (\exists n | n \in \text{adj}(v(x, y, z)), n \in N_c)\}. \quad (2)$$

There is the possibility that there may be more than one connected component  $A$  in the ROI that meets the threshold crite-

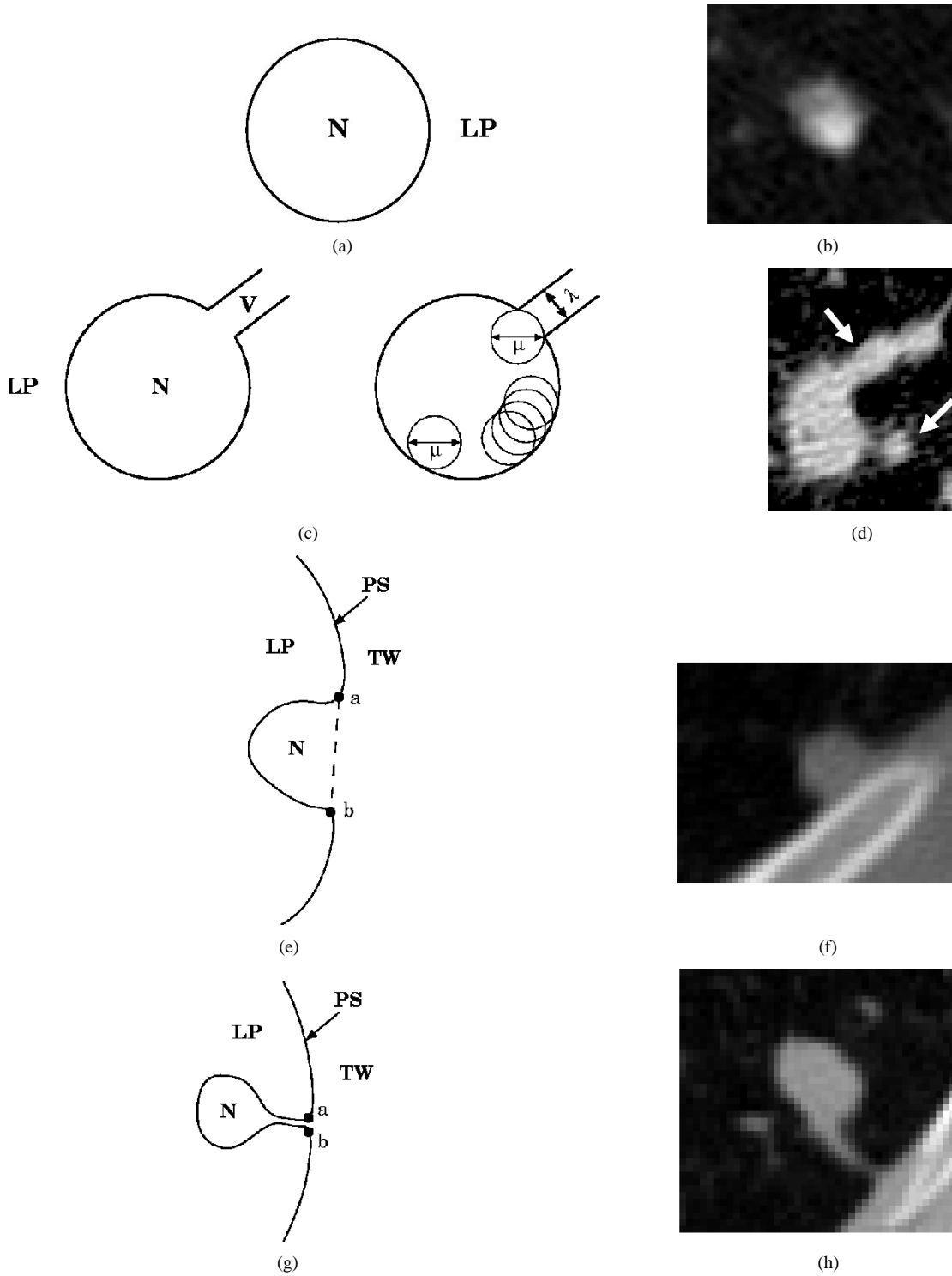


Fig. 2. Four classes of pulmonary nodules. (a) Well-circumscribed nodule model. (b) 5-mm well-circumscribed pulmonary nodule. (c) Vascularized pulmonary nodule model. (d) 7-mm pulmonary nodule with confounding vasculature. Arrows indicate the location of attached vessels. (e) Juxtapleural nodule model. (f) 5-mm juxtapleural nodule. (g) Pleural tail nodule model. (h) 9-mm pulmonary nodule with a pleural tail.

rion. We, therefore, elect to choose the largest of these sets  $N_{\max}$  (that which has the largest volume) as follows:

$$N_{\max} = \max A_i \quad (3)$$

where each of the eligible sets  $A_i$  is defined in an analogous manner to the definition of  $N_c$  in (2). Thus, we will assume that

the nodule will be the largest connected component (meeting the threshold criterion) in the ROI.

#### B. Vascularized

Measurement of the size and shape of pulmonary nodules is frequently confounded by the presence of other structures nearby or adjoining the nodule. Therefore, a simple two-level

model based on CT attenuation is insufficient to completely separate the pulmonary nodule under consideration from these other structures, as they frequently exhibit similar density characteristics. Fig. 2(d) shows an image of a small pulmonary nodule with surrounding and attached vessels. The attached vessels are indicated by white arrows.

A vascularized nodule is one that is located centrally in the lung, but has significant vascularization (connection to neighboring vessels). Clearly, the use of the well-circumscribed nodule model for the segmentation and analysis of vascularized nodules is inappropriate, as that model of connectivity would include the vascular components as part of the nodule. Instead, we define a model that distinguishes nodule volume from connected vessels geometrically.

Consider a model in which the vascularized nodule is the union of spheres of diameter  $\mu$  as follows:

$$N_v = \bigcup s(x, y, z) | d_s = \mu. \quad (4)$$

Each of the voxels in each one of these spheres must satisfy a threshold criterion, as was true for the well-circumscribed nodule model, as well as have no more than  $\mu/2$  distance from the sphere's center. The following equation describes such a sphere  $s(x, y, z)$  centered at voxel  $(x, y, z)$ , where  $D$  is the Euclidean distance function between two voxel locations:

$$s(x, y, z) = \bigcup \left\{ v(x_i, y_i, z_i) | (v(x_i, y_i, z_i) \geq T) \wedge \left( D(\{x_i, y_i, z_i\}, \{z, y, z\}) \leq \frac{\mu}{2} \right) \right\}. \quad (5)$$

We will additionally define a maximum diameter  $\lambda$  of any vessels that may be connected to the nodule volume. If we then choose  $\mu$  such that  $\mu > \lambda$ , we ensure that the majority of each vessel volume will not be included in the nodule volume.

This model of a vascularized nodule is illustrated in two dimensions in Fig. 2(c). The illustration on the left shows all of the nodule region  $N$  and vessel region  $V$  that meet the thresholding criterion. The illustration on the right shows how the nodule volume can be described as the union of circles (spheres in 3-D) of diameter  $\mu$ , while effectively ignoring the majority of the vascular component. The model of a vascularized nodule as a union of translated spheres is closely allied with the notion of the opening operation in mathematical morphology, which leads to segmentation methods described in Section IV. One of the issues of interest is the overestimation of nodule volume at the point of vessel attachment, as illustrated in Fig. 3(a). Note how the spherical "structuring element" allows the inclusion of a small amount of the vessel volume (outside the spherical nodule volume).

For an idealized model of a spherical nodule with a vascular attachment of diameter  $\lambda$ , it is possible to formally state the extent of this volume overestimation. The volume in the extraneous region  $V_{\text{ext}}$  is the difference between the portion (spherical cap)  $\hat{V}_\mu$  of the structuring element that extends beyond the line of length  $\lambda$  and the spherical cap  $\hat{V}_s$  of the spherical nodule volume beyond the same line. These two regions are illustrated (in 2-D) in the right-hand side of Fig. 3(a). The extraneous region  $V_{\text{ext}}$  is that between the dotted line (the boundary of the

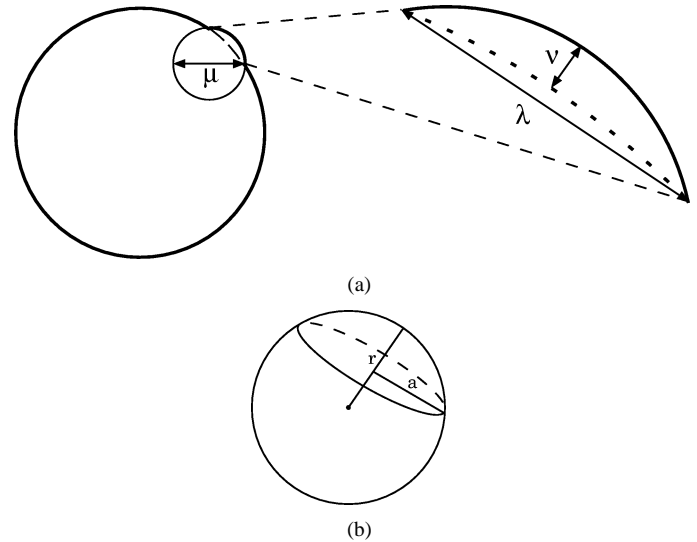


Fig. 3. Volume overestimation in a vascularized nodule. (a) Structuring kernel at the point of vascular attachment. (b) Volume of a spherical cap.

large sphere) and the external boundary. The largest perpendicular distance in this cup-shaped volume is shown as  $\nu$ . The volume  $\hat{V}_\mu$  is the region between the straight line of length  $\lambda$  and the external boundary, while the volume  $\hat{V}_s$  is that between the straight line and the dotted boundary of the large sphere. Therefore, the extraneous cup-shaped volume is simply their difference

$$V_{\text{ext}} = \hat{V}_\mu - \hat{V}_s. \quad (6)$$

Fig. 3(b) illustrates the volume of a spherical cap. The volume as a function of  $r$ , the radius of the sphere, and  $a$ , the radius of the intersecting disk, is

$$\hat{V}(r, a) = \frac{\pi}{3} \left( r - \sqrt{r^2 - a^2} \right)^2 \left( 2r - \sqrt{r^2 - a^2} \right). \quad (7)$$

Using (7), we may substitute the appropriate values of  $r$  and  $a$  to derive the volumes of  $\hat{V}_\mu$  and  $\hat{V}_s$ , and subsequently,  $V_{\text{ext}}$ . For the structuring sphere of radius  $\mu/2$ , the volume of the spherical cap is

$$\hat{V}_\mu = \frac{\pi}{3} \left( \frac{\mu}{2} - \sqrt{\left(\frac{\mu}{2}\right)^2 - \left(\frac{\lambda}{2}\right)^2} \right)^2 \cdot \left( \mu - \sqrt{\left(\frac{\mu}{2}\right)^2 - \left(\frac{\lambda}{2}\right)^2} \right) \quad (8)$$

and for the large sphere of radius  $r_s$ , the volume of the corresponding spherical cap is

$$\hat{V}_s = \frac{\pi}{3} \left( r_s - \sqrt{r_s^2 - \left(\frac{\lambda}{2}\right)^2} \right)^2 \left( 2r_s - \sqrt{r_s^2 - \left(\frac{\lambda}{2}\right)^2} \right). \quad (9)$$

The volume of the extraneous cup-shaped region, therefore, can be determined using (6), (8), and (9). Note that these expressions are general for any size spherical nodules, structuring spheres, and vessel diameters. More specifically, for a particular spherical nodule size and structuring sphere, the contribution of multiple vessels of different diameters can be determined. An example is illustrated in Fig. 4, where a spherical nodule of 8 mm

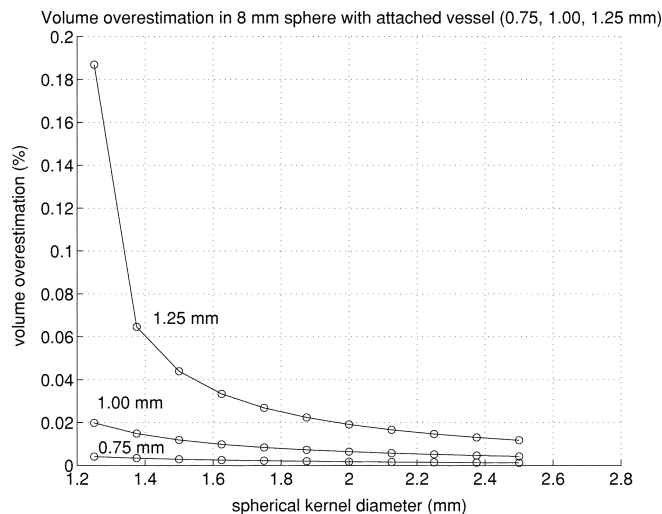


Fig. 4. Volume overestimation of an 8-mm spherical nodule with vascular attachments of varying sizes following opening with a spherical kernel.

in diameter ( $r = 4$ ) has a vascular attachment of varying diameter ( $\lambda$ ). Each of the curves in the graph corresponds to a  $\lambda$  value of 0.75, 1.0, or 1.25 mm. The graph illustrates the percent overestimation in nodule volume when the diameter of the structuring kernel used ( $\mu$ ) is varied from 1.25001 (slightly larger than  $\lambda$ ) to 2.5 mm. In the worst case ( $\lambda = 1.25$  mm,  $\mu = 1.25001$  mm), where the structuring kernel is barely large enough to detach the vessel, the volume overestimation is less than 0.19%. As the kernel diameter is increased, this value decreases logarithmically. Thus, given our model of a vascularized nodule, the union of spherical components, the minimum volume error in segmentation is achieved when the structuring kernel is as large as will fit the locally spherical region of the nodule.

### C. Juxtapleural

Peripheral pulmonary nodules often exhibit some degree of attachment to the pleural surface (on the periphery of the lung, compressed against the external boundary of the thorax). The majority of these nodules can be classified as juxtapleural. These nodules share a significant amount of their surface with the pleura. For this reason, delineation of the boundary between pleura and nodule can be quite challenging.

Fig. 2(e) illustrates a basic model of a juxtapleural nodule. The following four regions are defined:

- 1) N: nodule region;
- 2) LP: surrounding lung parenchyma;
- 3) PS: pleural surface;
- 4) TW: thoracic wall region.

An example of a small juxtapleural nodule is shown in Fig. 2(f). In CT images, the nodule and thoracic wall regions both exhibit high-attenuation characteristics. Therefore, while simple thresholding is able to separate the nodule from the lung parenchyma, it is insufficient to separate the nodule from the outer thoracic region. Anatomically, the pleural surfaces separate the lung volume (containing the parenchyma) and thoracic wall. When a juxtapleural nodule is present, however, there may or may not be invasion of the pleura. Whether the

nodule has invaded the pleura or is merely adjacent to it, voxel density (intensity) information is rarely sufficient to distinguish these regions.

In our model, we would like to consider the nodule region to be only that volume that is unlikely to be part of the thoracic wall. We define points  $a$  and  $b$  in the 2-D cross section shown in Fig. 2(e) to be those points of maximum concavity for a given scale. The notion of scale in the estimation of concavity here is quite important, as the pleural surface boundary is likely to have local concavities due to image sampling geometry and also pathologic or anatomic variation.

### D. Pleural Tail

A second class of pleurally attached nodules are those that exhibit the so-called “pleural tail sign.” This appears as a small thin structure of nodule-like attenuation connecting the nodule to the pleural surface, as illustrated in Fig. 2(g). A CT image of a nodule with a pleural tail is shown in Fig. 2(h). Although it would be simple to segment the majority of the nodule volume by using the vascular nodule segmentation algorithm to remove the pleural tail, in these cases, segmentation methods similar to those used for juxtapleural nodules should be employed. This is essential, as the volume of the “tail” is a component of the nodule volume and is not to be excluded, unlike similar looking vessels might be in vascularized nodules. If the vascular nodule segmentation algorithm were used, it would be impossible to quantify the growth of that portion of the lesion that comprises the tail.

## III. IMAGE ACQUISITION AND PREPROCESSING

The nodules studied here were initially detected on low-dose screening CT examinations [18], [19]. The tomographic image data for this study were subsequently acquired using GE High-Speed and LightSpeed CT scanners using a standard-dose protocol at 1 : 1 pitch small field of view 1–1.25-mm slice thickness, and 0.5-mm or better in-plane resolution [20], [21]. The nodule ROI for each case was identified by an experienced thoracic radiologist.

### A. Anisotropic Data

Most CT data are sampled in an anisotropic space, where the resolution in each of the three dimensions is not equal. The in-plane ( $x - y$ ) resolution on modern scanners is typically better than 1.0 mm in both dimensions. The axial ( $z$ ) resolution, however, may be anywhere from near 1 mm to as high as 20 mm. A typical high-resolution scan protocol provides 0.5-mm in-plane resolution with 1-mm axial reconstructions, producing voxels that are  $(0.5 \times 0.5 \times 1.0$  mm). This poses several problems. First, although high-resolution 2-D measurements can be made in any one of the highly resolved CT slices, 3-D measurements are hindered by the less-resolved axial dimension. Special anisotropic image filters need to take into account the different axial resolution, complicating 3-D analysis of the geometry of nodule and vascular components that may be present in any orientation. A second more important problem to consider is that of partial-volume effects.

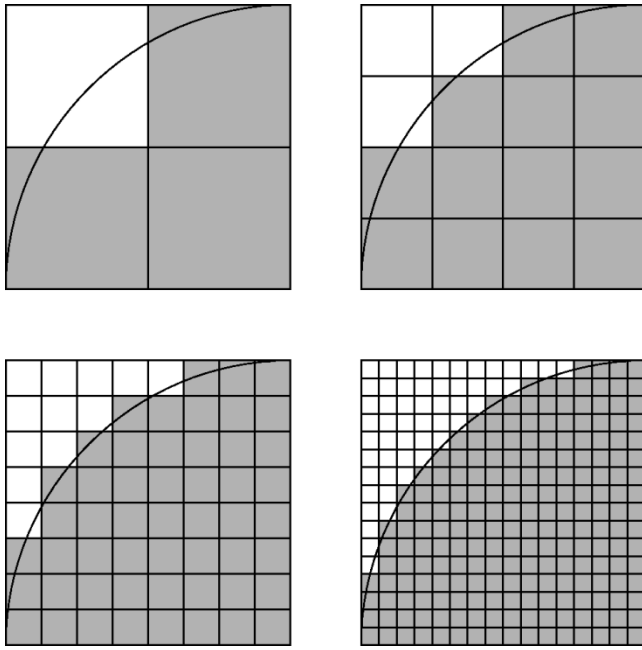


Fig. 5. 2-D area estimation of a segment of a circle. In each of the four illustrations, the segment is shown at successively higher degrees of resampling.

### B. Partial-Volume Problem

The partial-volume problem describes the quantized discrete spatial nature of the CT image. Consider the following 2-D example. A quadrant of a unit circle (radius = 1) is perfectly sampled on a regular grid. Pixels are set if 50% of their area corresponds to the interior of the circle. Initially, the quadrant is contained within a single pixel. The quadrant may then be divided, or *supersampled*, at any number of regular intervals to define an appropriate sampling grid, but for this example, we will restrict the number of divisions to be powers of two, with  $n$  the appropriate exponent of two. The degree of *resampling* of the image, or the supersampling ratio  $s$ , is the number of divisions of the original pixel size in each of the  $x$  and  $y$  dimensions

$$s_n = 2^n. \quad (10)$$

With this model in place, we may discuss the accuracy of area measurement of the circular segment as a function of sampling interval (image resolution). The true area of the circular segment is  $\pi/4 \approx 0.7854$ . In the case where  $n = 0$ , there is no resampling and the area is estimated to be 1.0. As  $n$  increases, the area estimates improve. For  $n = 1, 2, 3, 4$ , the corresponding area estimates are 0.75, 0.8125, 0.8125, and 0.7930 (Fig. 5). In this figure, pixels that would be considered members of the circle are shaded. It can be seen that, as the degree of subdivision of the sampling grid increases, the error in area estimation of the circle decreases. It is also possible to produce bounds for this error as a function of the degree of subdivision. Consider that the error in area estimation is only the sum of errors in pixels through which this circle boundary passes, each contributing either an overestimate or underestimate of the true area. The number of these boundary pixels  $b$  in this quadrant is defined as

$$b_n = 2^{n+1} - 1. \quad (11)$$

The first few terms in the sequence are 1, 3, 7, 15, 31. For example, in the lower left illustration in Fig. 5,  $n = 3$ ,  $s = 8$ , and  $b = 15$ .

As the contribution of each boundary pixel to the overall error is bounded by half the area of the pixel, a conservative upper bound on the error for estimating the area of the circular segment  $\epsilon$  can be expressed as

$$\epsilon = b \cdot \frac{a}{2} \quad (12)$$

where  $a$  is the area of a pixel. Given that this is a unit circle and, therefore, the quadrant has unit area, and that there are  $2^{2n}$  pixels in the quadrant, the area of each pixel is

$$a_n = \frac{1}{2^{2n}} = 2^{-2n}. \quad (13)$$

Thus, the error bound for a given value of  $n$  may be restated as the sequence where

$$\epsilon_n = b_n \cdot \frac{a_n}{2} = (2^{n+1} - 1) \cdot 2^{-(2n+1)} = \frac{1}{2^n} - \frac{1}{2^{2n+1}}. \quad (14)$$

Each of the two terms in this sequence converges to zero, with the latter converging much faster. Essentially, as  $n$  increases by one, the number of boundary pixels basically doubles, while their size and, thus, their error contribution, is divided by four. This leads to an error bound that is approximately halved with each increase in  $n$ . In three dimensions, the error is reduced by approximately a factor of eight with each increase in  $n$ .

### C. Isotropic Resampling

With this 2-D example, we can see how perfect interpolation, or resampling, of the image space can reduce errors in size estimation. Supersampling of the data has been implemented prior to segmentation in our analysis system. In addition, we supersample in different ratios to produce isotropic data. In three dimensions, isotropic resampling (supersampling to an isotropic space) allows segmentation decisions to be made on a super-resolved, or supersampled, grid, allowing more accurate consistent boundary decisions to be made. The intensity in each image voxel is interpolated to estimate the intensities in each of the subvoxels in the supersampled space. Thus, each original voxel intensity value is responsible for several in the new image space, mitigating partial-volume effects in the original data, as a more precise spatial location of the desired gray-level transition (boundary) can be identified. Fig. 6 illustrates some of the benefits of 3-D isotropic resampling using a small pulmonary nodule scanned at  $0.68 \times 0.68 \times 1.0$  mm resolution. Fig. 6(a) and (d) depicts transverse and coronal images revealing the isotropic nature of the original CT data. Fig. 6(b) and (c) compares transverse 3-D shaded surface representations of the segmented nodule before and after isotropic resampling to 0.25-mm cubic voxels, respectively. Fig. 6(e) and (f) compares the corresponding oblique 3-D shaded surface representations. In this example, the 3-D representation generated following the supersampling process [see Fig. 6(c) and (f)] illustrates the reduction in high-frequency spatial artifacts present in those derived from segmentation of the original data [see Fig. 6(b) and (e)] due to mitigation of the partial-volume problem.

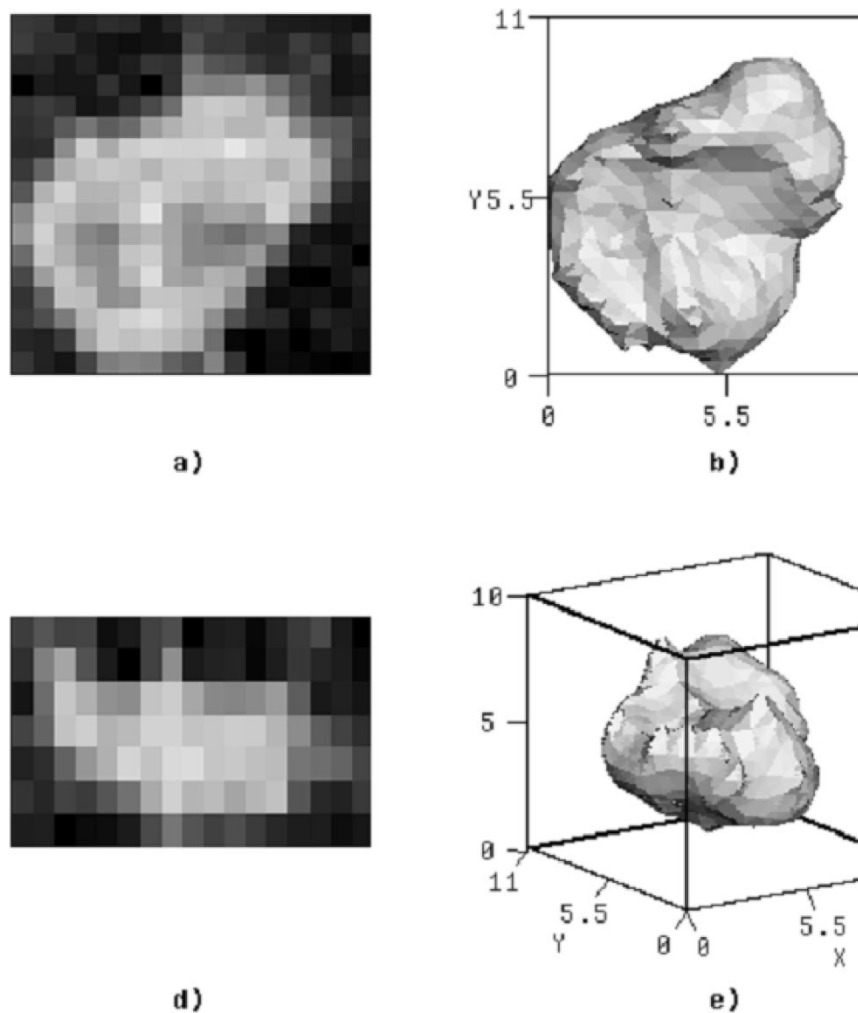


Fig. 6. Isotropic resampling of a small pulmonary nodule. Original CT image data in: (a) transverse and (d) coronal cross sections illustrate the anisotropic nature of the data. Transverse and oblique 3-D shaded surface representations of the nodule as segmented (b) and (e) before and (c) and (f) after isotropic resampling.

#### IV. SEGMENTATION

Segmentation is the most crucial and also most challenging step in the analysis of pulmonary nodules from CT image data. A helpful facet of this problem is the high degree of contrast between nodules and the much lower attenuating surrounding tissue. This would suggest intensity thresholding, region growing, or perhaps active contour approaches. However, delineation of the nodule boundary with respect to the surrounding lung parenchyma is only one of the challenges. Nodules are frequently attached to other structures, including the local pulmonary vasculature and the pleural surface adjoining the thoracic wall. The geometry of such attachments must be considered in order to successfully segment each type of nodule. We have developed mathematical models and methods for the segmentation of pulmonary nodules in each of these cases.

##### A. Thresholding

An important consideration when selecting a threshold for pulmonary nodule segmentation is that we are interested not only in making a single size determination of the nodule, but in evaluating its change in size over time. In order to make accurate

estimates of nodule growth, the segmentation should be consistent across multiple scans taken at different times. In growth estimation, the absolute error in size measurement is less significant than the relative error, considering multiple studies of the same nodule. This is due to the fact that growth estimates are computed based on size ratios, not on absolute size. For this reason, the same threshold value should be used in segmentation of each of the scans. Important caveats, however, are that the scanner must be well calibrated and the scan protocol (dose and resolution parameters) fixed for the observed attenuation values in each scan to be comparable.

It may also be beneficial to attempt a standard thresholding policy across nodules in different subjects. This is a more difficult problem, however, as mean nodule attenuation varies somewhat with nodule type. Nonsolid and part-solid nodules (lesions with mixed solid and nonsolid components), also known as ground glass opacities, frequently require a much lower threshold (or more than one) for accurate segmentation [22]. For the solid nodules considered in this study, a fixed threshold was used. It was determined based on phantom studies in which phantoms of known volumes were segmented and their volumes determined. The threshold that led to the most accurate and consistent volume measurements was

selected as the basis for segmentation of the nodules described in this paper.

A more general problem with global thresholding methods is that regions of similar intensity may be spatially disparate, and not represent components of the same object. For example, nearby vessels or other structures of nodule-like attenuation may be included in a thresholding-based segmentation. Image noise may also be of sufficient intensity to contribute to the output of a thresholding operation. These structures should not be included in the nodule region to be considered for further size and shape analysis.

### B. Connected Component Analysis

One solution to the problem of disparate high-intensity regions contributing to the segmented nodule volume is the use of connected component labeling and analysis [23]. The use of 3-D connected component analysis allows noise and extraneous structures to be removed from the nodule image data. The result of selecting a single connected component is an object that is contiguous in 3-D space.

In segmentation of pulmonary nodules, several selection criteria are commonly used in connected component analysis. These criteria are used to: 1) select the component of greatest volume; 2) select all components greater than or equal to a specified volume threshold; and 3) discard components within a specified distance of the ROI boundaries. These three criteria are used in the following way.

- 1) The object of greatest volume in the ROI is typically the nodule.
- 2) In some cases, more than one object of high relative volume in the ROI may need to be selected.
- 3) In segmentation of nodules near other large structures (e.g., pleural surface), the nodule may not be the object of greatest volume.

In these cases, the extraneous object is typically close to (or adjoining) the ROI boundary.

Thus, image thresholding and connected component analysis can be used for segmentation of pulmonary nodules when they are of relatively high intensity compared with the surrounding lung parenchyma. Such methods are insufficient, however, when nodules are attached to other structures of similar intensity (e.g., blood vessels). More advanced segmentation techniques are required for isolating the nodule volume in these cases.

### C. Morphological Processing

Methods for nodule segmentation can be developed based on global and/or local anatomical models. Of particular interest are the structures that may abut the nodule, such as pulmonary vessels or the pleural surface. We have developed specific segmentation methods for vascular nodules and for juxtapleural nodules based on the nodule models described in Section II and techniques from mathematical morphology [24]–[26].

1) *Vascular Subtraction*: Global methods for removing the pulmonary vasculature based on 3-D region-growing tree-traversal algorithms and other techniques have been described [27]–[29]. Other techniques for vascular segmentation in related

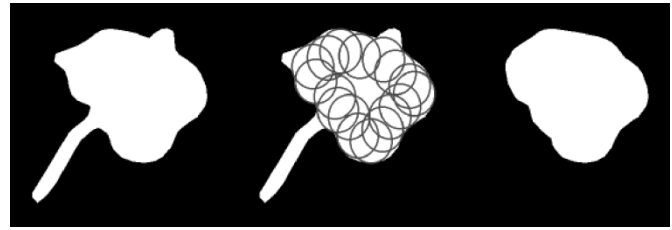


Fig. 7. Illustration of 2-D morphological opening on a pulmonary nodule. Note the removal of both the connected vessel and certain surface features.

applications have included time-of-flight magnetic resonance angiogram (MRA) segmentation based on adaptive statistical segmentation [30], active shape models for segmenting acute abdominal aneurysms [31], and a method for detection and measurement of vascular structures based on a Gaussian model [32].

The goal of global vascular segmentation methods is to simplify the nodule detection problem. For the characterization of pulmonary nodules using high-resolution data, however, local methods of vascular subtraction are more appropriate. Since only a small subset of the lung volume is normally acquired in a high-resolution diagnostic study, global methods tracing the vascular branches from the pulmonary artery and veins onward are impossible. Even if high-resolution data of the entire lung volume is available, this approach would likely be impractical. Furthermore, global or semiglobal region-growing schemes based on voxel intensity alone risk the removal of small nodules that exhibit vascular connections.

As an alternative to global region-growing techniques, we use a local filtering approach based on mathematical morphology. This method is based on the model described in Section II-B. The initial morphological processing in our segmentation algorithm consists of an opening operation based on a spherical kernel. This kernel is passed over the input data in a convolution-like filter for both the erosion and dilation steps, followed by connected component analysis to retain the nodule volume and discard vascular components that were initially disjoint or were disconnected via the opening operation.

One disadvantage of morphological opening in this application is that it has a “smoothing” effect on the nodule surface. Although the model indicates that the minimum volume error is achieved when the structuring kernel is as large as can be contained in the locally spherical region of the nodule, the size of locally spherical regions comprising *in vivo* nodules approaches zero in the limit. Thus, the structuring kernel that is large enough for vascular subtraction may also remove nodule surface details, such as fine spiculations. As an example, consider Fig. 7. The illustration on the left-hand side depicts a pulmonary nodule with a vascular attachment. In the center illustration, the translation of a circular kernel is shown, depicting a 2-D morphological opening operation. In the result shown on the right-hand side, notice that while the vessel has been removed (the desired effect), some of the surface features present in the original nodule have been deleted, as they were smaller than the structuring kernel.

While the need to remove vessels from consideration is important, we would prefer not to smooth away the very nodule



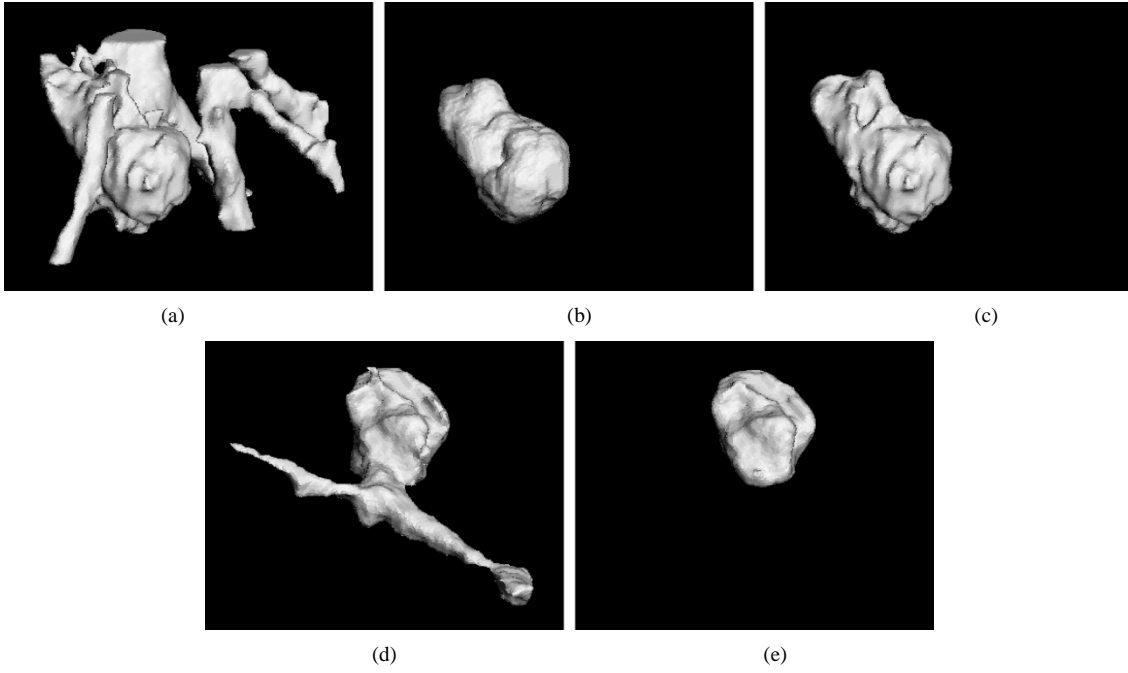


Fig. 8. Two *in vivo* examples of 3-D morphological filtering for vascular subtraction. (a) Basic threshold-based segmentation of a 7-mm pulmonary nodule. (b) Segmentation using 3-D morphological opening and connected component analysis, resulting in smoothing of nodule surface features. (c) Segmentation using vascular subtraction algorithm preserves nodule surface features. (d) and (e) Second example of vascular subtraction from a 6-mm pulmonary illustrating the point of vascular detachment.

surface characteristics we hope to analyze. To compensate for this smoothing effect, we may perform an iterative constrained dilation process to “regrow” these features. The entire morphological filtering process is as follows:

**Algorithm 1: Iterative Morphological Filtering**

```

Begin with an initial binary image  $I$ 
 $J = (I \ominus S_d) \oplus S_d$  {Opening using  $S_d$ }
Connected component analysis
 $s = d$ 
while  $s \geq 2$  {Number of useful dilations}
   $J = J \oplus S_s$  {Dilation using  $S_s$ }
   $J = J \wedge I$  {Voxel-by-voxel logical AND}
   $s = s/2$ 
end

```

Following morphological opening with a spherical kernel of diameter  $d$ ,  $S_d$ , this technique restores the detailed surface features of the nodule without regrowing vessels more than  $L = d$  voxels from the surface. In the first iteration, the dilation with a sphere of diameter  $d$  extends the surface at most  $d/2$  voxels in the direction of the vessel (as the spherical kernel  $S_s$  will only be replicated where its center exists in the input image  $J$ ). In each subsequent iteration, the surface may be extended by, at most, half the distance of the previous iteration. The upper bound on the growth of each vessel, therefore, is a distance of  $d$  voxels, as can be seen from the following geometric series:

$$L = \sum_{i=0}^{\log_2 d} \frac{d}{2^i} \simeq d. \quad (15)$$

In addition, the logical AND operation guarantees that all the features that are regrown were present in the initially thresholded image. Fig. 8(a)–(c) illustrates a comparison between the vascular subtraction using a morphological opening and connected component analysis with and without iterative filtering to regrow surface features. 3-D shaded surface representations of a small vascularized nodule are shown using different segmentation algorithms.

Fig. 8(a) shows the result of a basic segmentation method based on thresholding. Fig. 8(b) shows the result of a 3-D morphological opening using a spherical kernel of an appropriate size to remove the vessels connected to the nodule, as well as others in the ROI via connected-component analysis. Note that the surface of the segmented nodule is significantly smoothed when compared with the original thresholded data. In comparison, Fig. 8(c) illustrates the result of vascular subtraction via Algorithm 1, which adds the iterative morphological operations needed to regrow the nodule surface features. Note that the surface features present in the original thresholded data have been restored.

Fig. 8(d) and (e) shows another example of vascular subtraction via iterative morphological filtering. In this example, the major vascular component is removed, in addition to several minor vessels [note the small vessels protruding from the top surface of the threshold-segmented nodule (Fig. 8(d))]. Again, the vascular subtraction was achieved without a significant effect on desirable nodule surface features.

Note that the additional vessel growth allowed by this algorithm introduces more error than derived in Section II-B. In that discussion, we considered a simple model where a vascularized nodule was represented by the union of translated spheres of a fixed diameter, a model that can be realized with a single

opening operation. In the more complex algorithm described here, the use of iterative dilation operations with decreasing kernel sizes results in a somewhat larger error at the point of vascular attachment. This tradeoff is made to ensure the accurate representation of the other nodule surface features.

2) *Pleural Surface Removal*: A two-stage approach has been developed for the segmentation of juxta-pleural nodules. First, the orientation of the pleural surface in the ROI containing the nodule and associated section of the thoracic wall is determined using 3-D moment analysis [33], [34]. In this process, the ROI is thresholded and standard geometric moments of the first and second order ( $m_{pqr} | p + q + r \leq n$ ) are determined. The 3-D orientation of the ellipsoid of inertia (EOI) describing this region is then computed via the solution to the system  $Ax = \lambda x$  based on these moments where

$$A = \begin{pmatrix} m_{200} & m_{110} & m_{101} \\ m_{110} & m_{020} & m_{011} \\ m_{101} & m_{011} & m_{002} \end{pmatrix}. \quad (16)$$

The orthonormal basis of eigenvectors  $v_i$  produced in the solution of this problem points in the directions of each of the principal axes of the EOI. The eigenvalues  $\lambda_i$  are used to determine the lengths  $L_i$  of the three principal axes

$$L_i = 2\sqrt{\lambda_i} \cdot \sqrt[3]{\frac{3V}{4\pi\sqrt{\lambda_0\lambda_1\lambda_2}}}. \quad (17)$$

Using the eigenvectors, we can determine the Euler angles (roll, pitch, and yaw) describing the orientation of the nodule and thoracic wall) as functions of their projections on the  $YZ$ ,  $XZ$ , and  $XY$  planes, respectively,

$$\text{roll} = \cos^{-1} \left( \frac{\text{proj}_{YZ} v_2}{|v_2|} \right) \cdot \text{sign}(v_2(y)) \quad (18)$$

$$\text{pitch} = \cos^{-1} \left( \frac{\text{proj}_{XZ} v_0}{|v_0|} \right) \cdot \text{sign}(v_0(z)) \quad (19)$$

$$\text{yaw} = \cos^{-1} \left( \frac{\text{proj}_{XY} v_0}{|v_0|} \right) \cdot \text{sign}(v_0(y)). \quad (20)$$

This method is used to determine the angles describing the orientation of the pleural surface at the point where the juxta-pleural nodule is attached. Once this orientation has been determined, a structuring kernel is generated with the appropriate size and orientation (as determined by  $L_i$  and the dimensions of the ROI) such that an opening operation using this kernel can be used to detect the majority of the pleural surface and chest wall, while excluding the nodule. This kernel is disk-shaped (a cylinder with an elliptical cross section) and large enough so that it will fit only within the chest wall region and not the nodule portion of the image. 3-D image subtraction is then used to remove these external structures from the original image. Lastly, the remaining pleural components not detected in the opening operation are removed using an application of Algorithm 1. The complete method is described as Algorithm 2.

#### Algorithm 2: Pleural Surface Removal

Begin with an initial binary image  $I$   
 Determine orientation of the pleural surface  
 Generate a disk-shaped kernel  $D$ , oriented parallel to the pleural surface

$J = (I \ominus D) \oplus D$  {Opening using  $D$ }  
 $K = I - J$  {Image subtraction}  
 Continue with iterative morphological filtering {Alg. 1}

Two examples of the pleural surface removal technique are shown in Fig. 9. Fig. 9(a) shows a small nodule, approximately 5.5 mm in diameter, which is removed from the pleural surface [see Fig. 9(b)]. The segmentation process was as follows. The method of moments was used to compute the orientation of the pleural surface and attached nodule. Once the orientation of the pleural surface was determined, a disk-shaped kernel of 34 voxels (8.5 mm in cross-sectional length) was generated and used in a morphological opening to identify those voxels in the thoracic wall not containing the nodule. The pleural surface component was subsequently subtracted from the image, leaving the nodule and a small amount of pleural surface not identified by the opening operation. The resultant image was then segmented using iterative morphological filtering using a spherical kernel of 5 voxels (1.25 mm) in diameter to remove the remaining elements not belonging to the nodule volume. An additional example of this segmentation method on a 4-mm nodule is shown in Fig. 9(c) and (d).

3) *Algorithm and Parameter Selection*: Given the four classes of pulmonary nodules, the user should select the algorithm appropriate to each class. The vascular subtraction algorithm may be used both on vascularized nodules, as well as on those that are well circumscribed, as they represent the trivial case of vascularized nodules where the vessel diameters are below the effective resolution of the image. Similarly, the pleural surface removal algorithm can be used with both juxta-pleural nodules, as well as those with a pleural tail. Selection of the appropriate parameters for both the vascular subtraction algorithm and the pleural surface removal algorithm is critical to obtaining accurate nodule volume estimates. This topic will be addressed in Section IV.

## V. VOLUMETRIC DOUBLING TIME ESTIMATION

### A. Growth Model

Growth of early lung cancers is commonly modeled as an exponential growth process [35]–[37]. The tumor volume  $V$  can be expressed as a function of the initial volume  $V_0$

$$V = V_0 e^{\lambda t} \quad (21)$$

where the exponential coefficient  $\lambda$  may be defined with respect to the nodule *doubling time* (the time in days required for the tumor to double in volume) as

$$\lambda = \frac{\ln 2}{DT}. \quad (22)$$

### B. Doubling Time

Given two volumetric measurements of the lesion taken  $\Delta t$  days apart, we may estimate the doubling time using the following expression:

$$DT = \frac{\ln 2 \cdot \Delta t}{\ln \left( \frac{V_2}{V_1} \right)}. \quad (23)$$

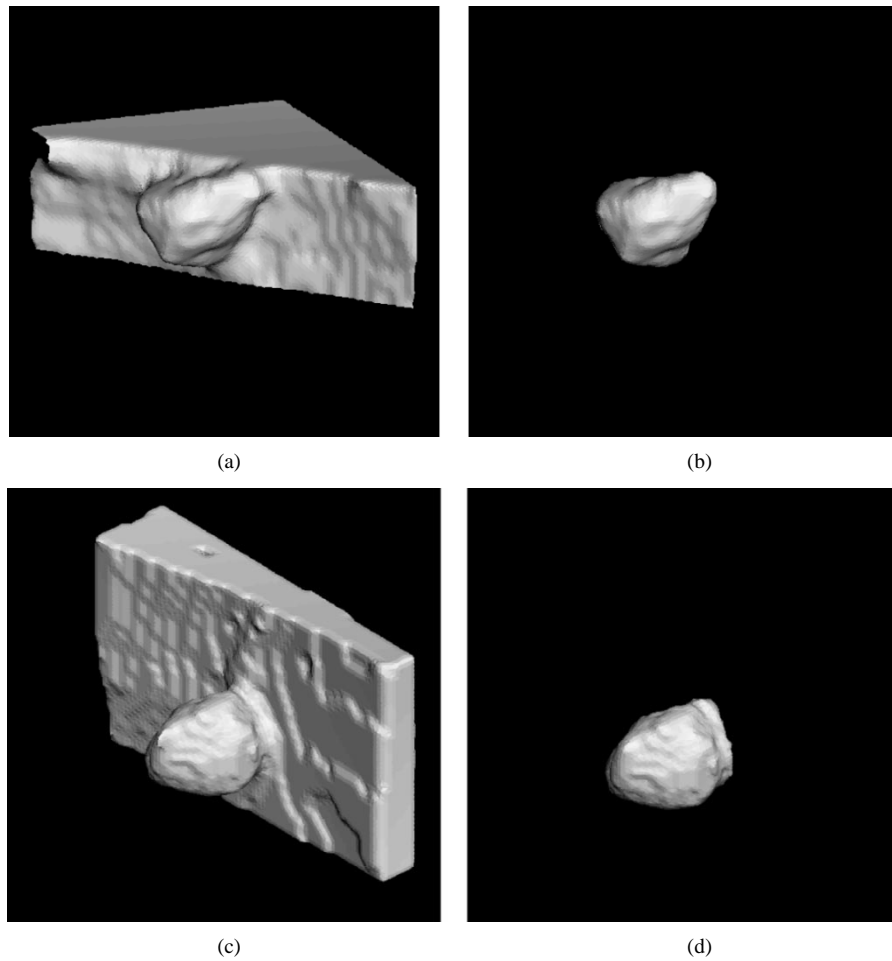


Fig. 9. Shaded surface representations of two juxtapleural nodules: (a) and (c) before and (b) and (d) after application of the pleural surface removal technique.

This expression compares directly with that used in the traditional 2-D analysis of nodule growth based on diametric measures on chest radiographs or single CT slices. In the 2-D case, there is an additional factor of three in the denominator (diameter varies as the cube root of volume) as follows:

$$DT_{2D} = \frac{\ln 2 \cdot \Delta t}{3 \ln \left( \frac{D_2}{D_1} \right)}. \quad (24)$$

Variation in slice selection, scanner/patient alignment, and asymmetric lesion growth are three factors that limit the accuracy of 2-D estimates of nodule doubling time.

3-D computer methods for the volumetric determination of nodule doubling times have been successfully used in the differentiation of benign from malignant lesions [11]. Of principal importance in this process, however, is the accurate reproducible segmentation of the nodules in each sequential scan.

### C. Error Estimation

We may estimate the variance of volumetric doubling-time estimation as a function of the error in each volume estimate  $\epsilon$  for a nodule of a given size in each scan. This can be determined experimentally using phantom studies [11] or alternatively using *in vivo* nodules with repeated imaging. While simple phantom studies allow us to quantify the effect of several sources of error (e.g., partial volume, threshold selection), there are other sources that are not taken into consideration. Among

these are the presence of motion artifacts due to respiration and the cardiac cycle. Quantification of these sources of error would require a large study of *in vivo* nodules, and is beyond the scope of this paper.

In this analysis, we will consider  $\epsilon$  to be the rms percent error in volume measurement, as determined experimentally. For this model, it is sufficient to use the rms percent error for a given nodule size rather than the maximum error, as we are estimating the underlying variation of the measurements rather than a conservative maximum error bound.

The volumetric doubling-time calculation is a nonlinear function of two volumetric measurements, which we will assume to be uncorrelated. In addition, it depends on the difference in time between scans  $\Delta t$ , which may introduce additional error as follows:

$$DT = f(V_1, V_2) = \frac{\ln 2 \cdot \Delta t}{\ln \left( \frac{V_2}{V_1} \right)}. \quad (25)$$

The error in a nonlinear function  $y = f(x_1, x_2, \dots, x_n)$  of uncorrelated variables can be estimated based on the variances of each variable. The exact differential [38] of  $y$

$$dy = \frac{\partial f}{\partial x_1} dx_1 + \frac{\partial f}{\partial x_2} dx_2 + \dots + \frac{\partial f}{\partial x_n} dx_n \quad (26)$$

leads to the argument that the variance in the function may be estimated by a sum of the contributions of the variances of each

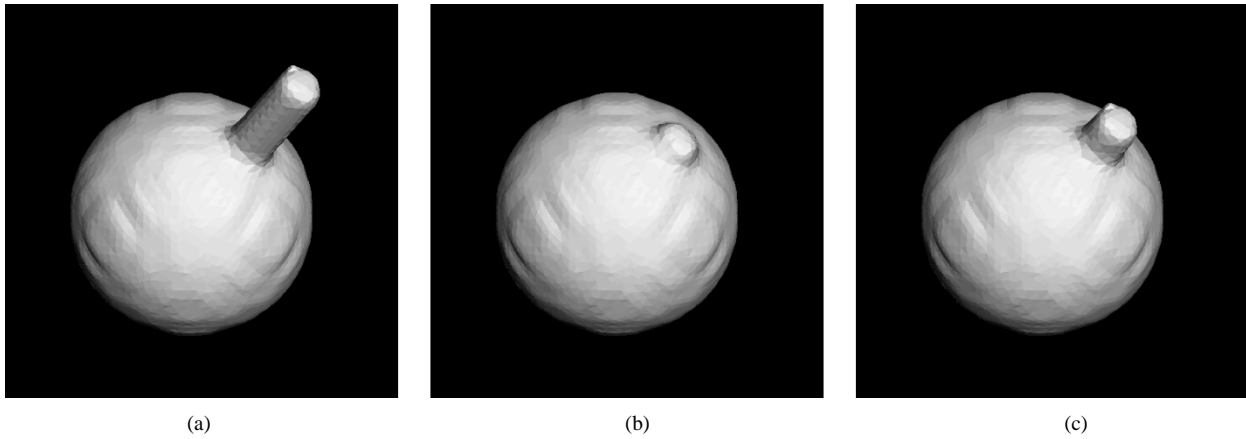


Fig. 10. Segmentation of a synthetic vascularized nodule using the vascular subtraction algorithm and structuring kernels of increasing diameter  $d$ : (a)  $d = 4$ ; (b)  $d = 5$ ; and (c)  $d = 12$ .

variable [39]. This is known as Gauss' law of error propagation. The variance in the nonlinear function above (if all  $x_i$  are uncorrelated) is

$$\sigma_y^2 = \left(\frac{\partial f}{\partial x_1}\right)^2 \sigma_{x_1}^2 + \left(\frac{\partial f}{\partial x_2}\right)^2 \sigma_{x_2}^2 + \cdots + \left(\frac{\partial f}{\partial x_n}\right)^2 \sigma_{x_n}^2. \quad (27)$$

In other words, the change (variance) in the function due to measurement error (as given by the exact differential) can be expressed as a function of the variance in measurement of each variable. We may, therefore, use this method to determine the variance of a particular doubling-time estimate, given estimates of the variance in each measurement  $V_1$ ,  $V_2$ , and  $\Delta t$ .

Starting from (25), we form the exact differential of the  $DT$  function

$$d(DT) = \frac{\ln 2}{\ln\left(\frac{V_2}{V_1}\right)} d(\Delta t) + \frac{\ln 2 \cdot \Delta t}{V_1 \left(\ln\left(\frac{V_2}{V_1}\right)\right)^2} d(V_1) + \frac{-\ln 2 \cdot \Delta t}{V_2 \left(\ln\left(\frac{V_2}{V_1}\right)\right)^2} d(V_2). \quad (28)$$

Using the law of error propagation, the variance in doubling-time estimation is then

$$\sigma_{DT}^2 = \left(\frac{\ln 2}{\ln\left(\frac{V_2}{V_1}\right)}\right)^2 \sigma_{\Delta t}^2 + \left(\frac{\ln 2 \cdot \Delta t}{V_1 \left(\ln\left(\frac{V_2}{V_1}\right)\right)^2}\right)^2 \sigma_{V_1}^2 + \left(\frac{-\ln 2 \cdot \Delta t}{V_2 \left(\ln\left(\frac{V_2}{V_1}\right)\right)^2}\right)^2 \sigma_{V_2}^2. \quad (29)$$

Interestingly, the variance of  $DT$  is not the appropriate error bound in this application. We would prefer, instead, to estimate the rms error of the measurement, which is equivalent to the standard deviation  $\sigma$  or the square root of the variance. For  $N$  measurements of variable  $x$ , these are equal to

$$\text{rms error} = \sigma = \sqrt{\frac{1}{N} \sum_{i=1}^N (x_i - \mu)^2} \quad (30)$$

and the rms error in doubling-time estimation is, therefore, simply the square root of (29). Thus, given an empirical estimate of  $\epsilon$ , the rms error in volume measurement as a function of nodule size (it will be different for  $V_1$  and  $V_2$ ) and an estimate of  $\sigma_{\Delta t}$  (which should be less than one day), we may estimate the variance and rms error of a particular doubling-time estimate produced by our method.

## VI. RESULTS

### A. Isotropic Resampling

Phantom experiments were performed to determine empirical values of our ability to reproducibly measure nodule volume based on isotropically resampling anisotropic CT data. Several experiments were done using small nodules imaged using CT data having  $0.2 \text{ mm} \times 0.2 \text{ mm} \times 1.0 \text{ mm}$  voxels. The data were isotropically supersampled to  $0.25\text{-mm}$  isotropic voxels using trilinear interpolation. The results of these experiments have been reported [11]. Briefly, measurements of 50 acrylic spheres of two diameters (3.96 and 3.20 mm) revealed that estimates of nodule volume could be made to within 2% rms error. In addition, an experiment using deformable synthetic nodules scanned before and after deformation indicated that, even in the presence of great variation in morphology, volume could be reproducibly measured to within 3% rms error.

### B. Segmentation

A sensitivity analysis was performed to assess the effect of two parameters of the vascularized nodule segmentation algorithm (Algorithm 1): the gray-level threshold and the structuring kernel diameter. Scans of the 50 acrylic nodule phantoms were segmented using varying thresholds and the resulting mean volume measurements calculated. A standard threshold was determined as that which produced the least variance from the expected volume of the spheres. We observed that variations in the threshold around the standard value resulted in variation in nodule volume by somewhat less than 0.2%/HU for the 3.96-mm spheres and somewhat less than 0.5%/HU for the 3.20-mm spheres. A similar experiment was performed on 21 *in vivo* pulmonary nodules using the vascular subtraction algorithm and a fixed structuring kernel diameter.

In this case, the variation of the error was similar for nodules of similar size to the phantoms and smaller for those of larger size due to the smaller proportion of surface voxels.

The diameter of the structuring kernel used in Algorithm 1 affects both the initial morphological opening of the scene, but also the sizes of kernels used to regrow the surface features. The most important consideration when choosing the kernel size is that the sizes of nodules and vessels vary, as described in our vascularized nodule model (Section II-B). In particular, the cross-sectional diameter of attached vessels ( $\lambda$  from our model) may vary considerably from case to case. Still, although we may choose a kernel of diameter  $d$  such that it is likely to be larger than most vessels, overestimation of the appropriate kernel size may lead to overestimation of the nodule volume at those points where considerably smaller vessels were attached. This relationship was expressed mathematically in (15), where the upper bound on “regrowth” of a vessel is bounded by the diameter of the structuring kernel  $d$ . A complete expression for this overestimate was derived for the spherical vascularized nodule model in (6), (8), and (9).

Here, we illustrate graphically for a 3-D synthetic model. In this example, a synthetic nodule was constructed having a diameter of 25 voxels with an attached vessel of 5 voxels in diameter. Given our standard 0.25-mm isotropically resampled data, this would correspond to a nodule diameter of 6.25 mm and vessel diameter of 1.25 mm, well within the typical range in this study.

Using this synthetic nodule, the diameter of the structuring element used in Algorithm 1 was varied and the resultant segmentations evaluated visually and numerically. Given the characteristics of the iterative vascular subtraction method, there are the following three regions in which values of this parameter may fall:

- $d$ : too small—the vessel is not removed;
- $d$ : in an acceptable range—the vessel is correctly removed;
- $d$ : too large—the vessel is removed, but regrown to a significant degree.

Three examples from this experiment are shown in Fig. 10. In the left image ( $d = 4$ ), the kernel is too small to remove the vessel in the initial morphological opening. In the center image, the kernel is in the acceptable range for a proper segmentation (in this case,  $d = 5$ ). In the right image, the kernel is somewhat too large, resulting in a significant amount of vessel “regrowth.”

An experiment was performed to assess the behavior of this segmentation technique using synthetic vascularized nodules (a sphere with vessels of varying diameters). These models were segmented using kernels of increasing size, and the degree of volume overestimation recorded. Fig. 11 shows the relative volume of the segmented nodule model as a function of vessel diameter  $d_v$  and kernel diameter  $d$ . Each of these parameters are expressed with respect to nodule spherical diameter  $d_s$ . The data for each vessel diameter are shown beginning with the kernel size that is sufficiently large to exclude the vessel.

These data show that, although the degree of volume overestimation increases with kernel size (over the minimum diameter required to exclude the vessel), the effect is still within 4% for kernels as large as 60% of the diameter of the nodule and for vessels as large as 30% the nodule. Still, the overall goal is to

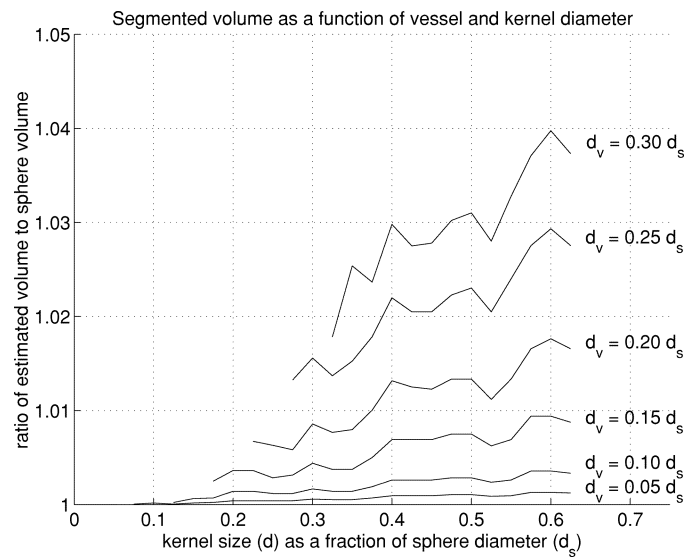


Fig. 11. Dependence of vascular subtraction as a function of vessel diameter  $d_v$  and kernel size  $d$  for spherical synthetic nodules of diameter  $d_s$ .

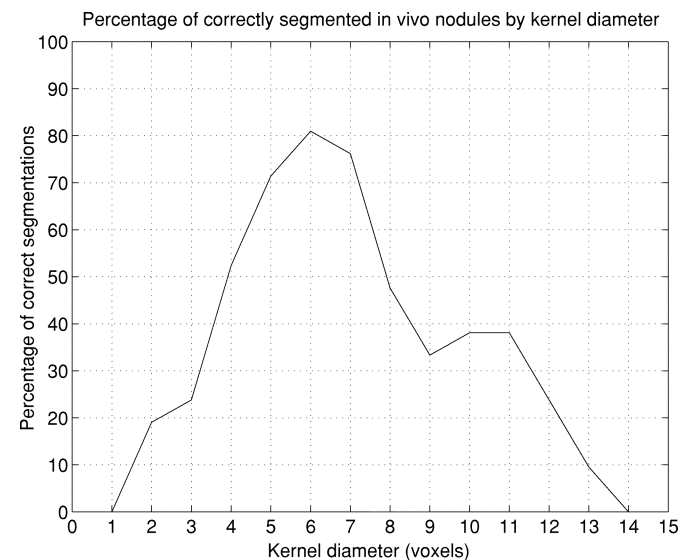


Fig. 12. Dependence of vascular subtraction on structuring kernel diameter in segmenting *in vivo* pulmonary nodules.

identify that range of kernel sizes that leads to good nodule segmentation for a wide variety of *in vivo* nodules.

To this end, an additional experiment was performed to test the dependence of the vascular subtraction technique on structuring kernel diameter in 21 *in vivo* pulmonary nodules. For each nodule, the diameter of the structuring kernel  $d$  was varied from 1 to 20 voxels. In each of the resultant segmentations, the degree to which the vessel or vessels (most nodules had more than one vascular attachment) were removed was evaluated. A nodule segmentation was considered to be “correct” when its volume was within 5% of the best segmentation possible, as determined by the reviewing radiologist.

Fig. 12 illustrates the result of this experiment. The graph shows the relationship between structuring kernel diameter and the percentage of nodules correctly segmented. Recall that, for

TABLE I  
In Vivo NODULE DOUBLING TIMES BASED ON CHANGE IN VOLUME AND AREA MEASUREMENTS

Case	$\Delta t$	$d_0$ (mm)	Volume (mm <sup>3</sup> )		Area (mm <sup>2</sup> )		$DT$ (days)		Status
			$t_0$	$t_1$	$t_0$	$t_1$	Volume	Area	
1	36	6.9	106.9	135.7	36.5	36.6	104	9700	Malignant
2	20	9.3	239.8	313.8	65.9	74.1	51	78	Malignant
3	69	5.4	141.3	184.8	18.1	25.7	177	90	Malignant
4	71	6.5	265.2	466.4	32.6	66.9	87	46	Malignant
5	33	5.5	62.5	85.3	250.1	341.2	73	49	Malignant
6	745	3.9	89.0	166.4	11.4	28.3	826	378	Non-malignant
7	35	7.4	70.0	70.9	280.1	283.4	2030	135	Non-malignant
8	35	7.2	54.6	56.3	218.5	225.3	798	532	Non-malignant
9	84	4.1	36.2	36.2	13.0	14.9	33700	288	Non-malignant
10	225	4.0	41.5	37.6	12.2	11.8	-1570	-2840	Non-malignant
11	61	7.1	208.6	219.3	38.9	46.3	846	164	Non-malignant
12	70	8.4	207.9	222.2	52.4	53.6	731	1520	Non-malignant
13	306	5.8	91.5	156.2	25.6	34.1	396	494	Non-malignant
14	128	4.2	49.6	65.6	14.0	17.5	318	265	Non-malignant
15	140	11.9	507.8	494.3	109.8	106.1	-3610	-1890	Non-malignant
16	111	4.6	36.7	26.7	146.9	106.9	-242	-161	Non-malignant

a given nodule and set of attached vessels, there are usually a range of values of  $d$  that lead to a correct segmentation.

In these results, we may note that over 80% of the *in vivo* vascularized nodules were correctly segmented by using a fixed structuring kernel diameter of six voxels (1.5 mm). The graph also exhibits a somewhat bimodal appearance. Inspection of the data reveals that, while the majority of vascularized nodules studied were connected to vessels smaller than 2 mm in diameter, there was an additional group of nodules with larger vascular components, resulting in the secondary peak at  $d = 10$ . Therefore, although a static structuring kernel size may be chosen that yields reasonably good results over a wide range of nodules, a better approach is to choose a structuring kernel of the appropriate size for a particular case. When manually selecting the appropriate kernel size for each case, all but one (95%) of the nodules in this experiment were correctly segmented. In this last case, manual editing of the nodule boundary was necessary to produce a correct segmentation.

The success of the pleural surface removal algorithm is somewhat dependent on the geometry of the nodule ROI. This is due to the fact that estimation of the orientation of the nodule-pleura interface is based on moment calculations involving the thresholded ROI. In experiments performed on 18 *in vivo* juxtapleural nodules, Algorithm 2 was able to perform a correct segmentation in 13 (72%) of the cases. When a user was able to manually specify the orientation of the disk, the results improved, allowing for correct segmentation in 15 (83%) of the cases. In the remainder of the cases, manual segmentation was required. These cases were located in the lung apices or where the assumption of local planarity of the chest wall is less valid. Overall, the results are promising in that they offer a consistent automated segmentation technique for the majority of juxtapleural nodules seen in this study.

In the implementation of our system described in this paper, the parameters for both the vascular subtraction and pleural surface removal algorithms are set to default values that have been seen to produce the best results on the wide range of nodules tested. When the segmentation results are unacceptable to the reviewing radiologist, the user has the ability to alter the values of

these parameters and recompute the segmentation. This procedure is typically sufficient to produce an accurate segmentation of the large majority of nodules, as described above. Our current development efforts include methods to automate the selection of segmentation parameters based on initial analysis of nodule size, location, and vascular geometry. For example, given an estimate of the diameter of the nodule and each of the attached vessels, the appropriate diameter for the structuring kernel in the vascular subtraction algorithm can be determined.

### C. Growth Assessment

The first experiment performed to evaluate our doubling-time-estimation methods was designed to compare the differences in doubling-time estimates based on 2-D areal and 3-D volumetric measurements. The 3-D measurements were made using the techniques outlined in this paper. For comparison, doubling times were also computed based on the area of the axial slice of maximum cross-sectional area in each nodule based on the same 3-D segmentation used to produce the volume measurements.

Two high-resolution CT studies were obtained for each of 16 (five malignant, 11 nonmalignant) small pulmonary nodules. These included three well-circumscribed nodules, nine vascularized nodules, three juxtapleural nodules, and one pleural tail nodule. All cases for this study were taken from our lung cancer screening program. Information regarding the size of the overall Early Lung Cancer Action Project study, as well as the prevalence of nodules and malignancy, has been reported in the literature [18], [19]. The nodules were classified as malignant by cytologic or histologic diagnosis, whereas the nonmalignant nodules were classified by a specific benign diagnosis on cytology or by exhibiting no radiographic change over more than two years. Each of the cases were segmented using the techniques described in Section IV. Manual adjustment of the kernel size used for vascular subtraction (Algorithm 1) was deemed necessary by the radiologist in two cases, as was adjustment of the orientation of the disk for Algorithm 2 in one case.

The initial diameter of each of the nodules at  $t_0$ ,  $d_0$  was determined as the average of the major and minor principal axes of the ellipse of inertia describing the segmented nodule in the slice of maximum cross-sectional area. This measure was used instead of the average of the three principal axes of the EOI describing the entire nodule, as it more closely corresponds with traditional radiographic assessment. The median diameter at  $t_0$ ,  $\hat{d}_0$  was 6.2 mm. The time interval between the scans  $\Delta t$  ranged from 20 to 71 days (median = 36 days) for the malignant nodules and from 35 to 745 days (median = 111 days) for the nonmalignant nodules. The results are shown in Table I.

Volumetrically determined doubling times for the malignant nodules ranged from 51 to 177 days. Doubling times for most malignant nodules range from 30 to 400 days, and these cases were all well within this range [40]. Similarly, doubling times for the nonmalignant nodules ranged from 318 to 33 700 days for growing nodules and from -242 to -3610 for those nodules that were found to have reduced in volume on repeat examination. With the exception of Case 14, all nonmalignant nodules had doubling times consistent with benignity.

Doubling times based on maximum cross-sectional area did not agree as well with previously reported values for pulmonary malignancy. Four of the nonmalignant cases had doubling times that fall within the range of those for typical lung cancers.

## VII. CONCLUSION

3-D methods can be used in the effective segmentation and volumetric measurement of small pulmonary nodules imaged using high-resolution CT. We have described algorithms we developed for the different morphologic classes of pulmonary nodules, including well-circumscribed, vascularized, and juxtapleural nodules.

Experiments were performed to assess the ability of the 3-D methods to estimate nodule growth rate and were shown to be more accurate than those based on 2-D measurements. Volumetrically determined estimates of nodule doubling time in malignant nodules were consistent with those reported in the literature. All but one of the nonmalignant nodules had doubling times typical of benign species.

Further development of these methods is currently underway, including studies of the effect of varying scan parameters on doubling-time estimates, as well as clinical validation on larger datasets. With improving CT resolution, we hope to improve our ability to estimate nodule growth rate and study other nodule characteristics such as shape and density distribution.

## REFERENCES

- [1] R. T. Greenlee, M. B. Hill-Harmon, T. Murray, and M. Thun, "Cancer statistics, 2001," *Cancer J. Clinicians*, vol. 51, no. 1, pp. 15–36, Jan.–Feb. 2001.
- [2] M. L. Giger, K. T. Bae, and H. MacMahon, "Computerized detection of pulmonary nodules in computed tomography images," *Investigat. Radiol.*, vol. 29, no. 4, pp. 459–465, Apr. 1994.
- [3] S. Toshioka, K. Kanazawa, N. Niki, H. Satoh, H. Ohmatsu, K. Eguchi, and N. Moriyama, "Computer aided diagnosis system for lung cancer based on helical CT images," *Proc. SPIE*, vol. 3034, pp. 975–984, Feb. 1997.

- [4] M. F. McNitt-Gray, E. M. Hart, N. Wyckoff, J. W. Sayre, J. G. Goldin, and D. R. Aberle, "A pattern classification approach to characterizing solitary pulmonary nodules imaged on high resolution CT: Preliminary results," *Med. Phys.*, vol. 26, no. 6, pp. 880–888, June 1999.
- [5] B. Zhao, D. F. Yankelevitz, A. P. Reeves, and C. I. Henschke, "Two-dimensional multi-criterion segmentation of pulmonary nodules on helical CT images," *Med. Phys.*, vol. 26, no. 6, pp. 889–895, June 1999.
- [6] D. F. Yankelevitz, R. Gupta, B. Zhao, and C. I. Henschke, "Small pulmonary nodules: Evaluation with repeat CT—preliminary experience," *Radiology*, vol. 212, no. 2, pp. 561–566, Aug. 1999.
- [7] Y. Kawata, N. Niki, H. Ohmatsu, K. Eguchi, and N. Moriyama, "Shape analysis of pulmonary nodules based on thin section CT images," *Proc. SPIE*, vol. 3034, pp. 964–974, Feb. 1997.
- [8] B. Zhao, W. J. Kostis, A. P. Reeves, D. F. Yankelevitz, and C. I. Henschke, "Consistent segmentation of repeat CT scans for growth assessment in pulmonary nodules," *Proc. SPIE*, vol. 3661, pp. 1012–1018, Feb. 1999.
- [9] A. P. Reeves, W. J. Kostis, D. F. Yankelevitz, and C. I. Henschke, "Three-dimensional shape characterization of solitary pulmonary nodules from helical CT scans," in *Proc. Computer Assisted Radiology and Surgery (CARS '99)*, H. U. Lemke, M. W. Vannier, K. Inamura, and A. G. Farman, Eds., pp. 83–87.
- [10] S. G. Armato, III, M. L. Giger, C. J. Moran, J. T. Blackburn, K. Doi, and H. MacMahon, "Computerized detection of pulmonary nodules on CT scans," *Radiographics*, vol. 19, no. 5, pp. 1303–1311, Sept.–Oct. 1999.
- [11] D. F. Yankelevitz, A. P. Reeves, W. J. Kostis, B. Zhao, and C. I. Henschke, "Small pulmonary nodules: Volumetrically determined growth rates based on CT evaluation," *Radiology*, vol. 217, no. 1, pp. 251–256, Oct. 2000.
- [12] M. F. McNitt-Gray, N. Wyckoff, J. G. Goldin, R. Suh, J. W. Sayre, and D. R. Aberle, "Computer-aided diagnosis of the solitary pulmonary nodule imaged on CT: 2D, 3D, and contrast enhancement features," *Proc. SPIE*, vol. 4322, pp. 1845–1852, Feb. 2001.
- [13] K. Minami, Y. Kawata, N. Niki, K. Mori, H. Ohmatsu, R. Kakinuma, K. Eguchi, M. Kusumoto, M. Kaneko, and N. Moriyama, "Computerized characterization of contrast enhancement patterns for classifying pulmonary nodules," *Proc. SPIE*, vol. 4322, pp. 1936–1948, Feb. 2001.
- [14] M. S. Brown, M. F. McNitt-Gray, J. G. Goldin, R. D. Suh, J. W. Sayre, and D. R. Aberle, "Patient-specific models for lung nodule detection and surveillance in CT images," *IEEE Trans. Med. Imag.*, vol. 20, pp. 1242–1250, Dec. 2001.
- [15] J. P. Ko and M. Betke, "Chest CT: Automated nodule detection and assessment of change over time—preliminary experience," *Radiology*, vol. 218, no. 1, pp. 267–273, Jan. 2001.
- [16] S. J. Swensen, M. D. Silverstein, D. M. Ilstrup, C. D. Schleck, and E. S. Edell, "The probability of malignancy in solitary pulmonary nodules. Application to small radiologically indeterminate nodules," *Arch. Intern. Med.*, vol. 157, no. 8, pp. 849–855, Apr. 1997.
- [17] J. W. Gurney, "Determining the likelihood of malignancy in solitary pulmonary nodules with Bayesian analysis. Part I. Theory," *Radiology*, vol. 186, no. 2, pp. 405–413, Feb. 1993.
- [18] C. I. Henschke, D. I. McCauley, D. F. Yankelevitz, D. P. Naidich, G. McGuinness, O. S. Miettinen, D. M. Libby, M. W. Pasmantier, J. Koizumi, N. K. Altorki, and J. P. Smith, "Early lung cancer action project: Overall design and findings from baseline screening," *Lancet*, vol. 354, no. 9173, pp. 99–105, July 1999.
- [19] C. I. Henschke, D. P. Naidich, D. F. Yankelevitz, G. McGuinness, D. I. McCauley, J. P. Smith, D. Libby, M. Pasmantier, M. Vazquez, J. Koizumi, D. Flieder, N. Altorki, and O. S. Miettinen, "Early lung cancer action project: Initial findings on repeat screenings," *Cancer*, vol. 92, no. 1, pp. 153–159, July 2001.
- [20] W. A. Kalender, "Technical foundations of spiral CT," in *Seminars Ultrasound, CT, and MRI*, vol. 15, Apr. 1994, pp. 81–89.
- [21] H. Hu, "Multi-slice helical CT: Scan and reconstruction," *Med. Phys.*, vol. 26, no. 1, pp. 5–18, Jan. 1999.
- [22] C. I. Henschke, D. F. Yankelevitz, R. Mirtcheva, G. McGuinness, D. McCauley, and O. S. Miettinen, "CT screening for lung cancer: Frequency and significance of part-solid and nonsolid nodules," *Amer. J. Roentgenol.*, vol. 178, no. 5, pp. 1053–1057, May 2002.
- [23] R. C. Gonzales and R. E. Woods, *Digital Image Processing*. Reading, MA: Addison-Wesley, 1992.
- [24] J. Serra, *Image Analysis and Mathematical Morphology*. London, U.K.: Academic, 1982.
- [25] —, *Image Analysis and Mathematical Morphology. Volume 2: Theoretical Advances*. London, U.K.: Academic, 1988.
- [26] A. K. Jain, *Fundamentals of Digital Image Processing*. Englewood Cliffs, NJ: Prentice-Hall, 1989.

- [27] S. A. Wood, E. A. Zerhouni, J. D. Hoford, E. A. Hoffman, and W. Mitzner, "Measurement of three-dimensional lung tree structures by using computed tomography," *J. Appl. Phys.*, vol. 79, no. 5, pp. 1687–1697, Nov. 1995.
- [28] P. Croisille, M. Souto, M. Cova, S. Wood, Y. Afework, J. E. Kuhlman, and E. A. Zerhouni, "Pulmonary nodules: Improved detection with vascular segmentation and extraction with spiral CT," *Radiology*, vol. 197, no. 2, pp. 397–401, Nov. 1995.
- [29] M. Sonka, G. Sundaramoorthy, and E. A. Hoffman, "Knowledge-based segmentation of intrathoracic airways from multidimensional high resolution CT images," *Proc. SPIE*, vol. 2168, pp. 73–85, Aug. 1994.
- [30] D. L. Wilson and J. A. Noble, "An adaptive segmentation algorithm for time-of-flight MRA data," *IEEE Trans. Med. Imag.*, vol. 18, pp. 938–945, Oct. 1999.
- [31] M. de Bruijne, B. van Ginneken, W. J. Niessen, J. B. A. Maintz, and M. A. Viergever, "Active shape model based segmentation of abdominal aortic aneurysms in CTA images," *Proc. SPIE*, vol. 4684, pp. 463–474, Feb. 2002.
- [32] K. Krissian, G. Malandain, N. Ayache, R. Vaillant, and Y. Troussset, "Model-based detection of tubular structures in 3D images," *Comput. Vis. Image Understanding*, vol. 80, no. 2, pp. 130–171, Nov. 2000.
- [33] A. P. Reeves and B. S. Wittner, "Shape analysis of three dimensional objects using the method of moments," in *Proc. IEEE Computer Vision Pattern Recognition Conf.*, June 1983, pp. 20–26.
- [34] A. P. Reeves, R. J. Prokop, S. E. Andrews, and F. P. Kuhl, "Three-dimensional shape analysis using moments and Fourier descriptors," *IEEE Trans. Pattern Anal. Machine Intell.*, vol. 10, pp. 937–943, Nov. 1988.
- [35] M. Schwartz, "A biomathematical approach to clinical tumor growth," *Cancer*, vol. 14, no. 6, pp. 1272–1294, Nov.–Dec. 1961.
- [36] K. Usuda, Y. Saito, M. Sagawa, M. Sato, K. Kanma, S. Takahashi, C. Endo, Y. Chen, A. Sakurada, and S. Fujimura, "Tumor doubling time and prognostic assessment of patients with primary lung cancer," *Cancer*, vol. 74, no. 8, pp. 2239–2244, Oct. 1994.
- [37] J. S. Spratt, J. S. Meyer, and J. A. Spratt, "Rates of growth of human solid neoplasms: Part II," *J. Surgical Oncol.*, vol. 61, no. 1, pp. 68–83, Jan. 1996.
- [38] G. Birkhoff and G.-C. Rota, *Ordinary Differential Equations*, 2nd ed. New York: Wiley, 1989.
- [39] J. R. Taylor, *An Introduction to Error Analysis: The Study of Uncertainties in Physical Measurements*. Mill Valley, CA: Univ. Sci. Books, 1982.
- [40] G. A. Lillington, "Management of solitary pulmonary nodules," *Postgraduate Med.*, vol. 101, no. 3, pp. 145–150, Mar. 1997.